Energy & Environmental Science

ROYAL SOCIETY OF CHEMISTRY

PAPER

View Article Online
View Journal

Check for updates

Cite this: DOI: 10.1039/d0ee03679j

Advanced manufacturing for electrosynthesis of fuels and chemicals from CO_2†

Daniel Corral, ‡[ab] Jeremy T. Feaster, ‡[c] Sadaf Sobhani, [d] Joshua R. DeOtte, [a] Dong Un Lee,[b] Andrew A. Wong, [a] Julie Hamilton,[a] Victor A. Beck, [d] Amitava Sarkar, [bce] Christopher Hahn, *[f] Thomas F. Jaramillo, *[bf] Sarah E. Baker*[c] and Eric B. Duoss *[a]

Received 21st November 2020,
Accepted 3rd February 2021

DOI: 10.1039/d0ee03679j

rsc.li/ees

Advanced manufacturing (AM) represents an appealing approach for creating novel electrochemical systems for chemicals synthesis. In this work, we demonstrate AM for rapid development and testing for improved performance for the carbon dioxide reduction reaction across an evolution of vapor-fed reactor designs. In our final design, we observe activation- and mixed-control regimes for a variety of operating conditions *via* inlet CO_2 flow rate and electrochemical potential. Furthermore, we define a dimensionless number (Da) to identify mass transport regimes by exploring the impact of hypothesized underlying mass transport mechanisms, including consumption of CO_2 *via* OH^-, increased local temperatures, and partial penetration of electrolyte into gas diffusion layer. The accelerated pace of reactor design and development led to high geometric current densities (500 mA cm^{-2}), heightened selectivity (85.5% FE C_{2+} products), and increased carbon dioxide conversion (16.6%) and cathodic energy efficiency (49.6% CO_2R). Using AM vapor-fed reactors, we attain high ethylene (3.67%) and record ethanol (3.66%) yields compared to the literature. This work underscores the promise of AM for accelerating reactor design, understanding of governing phenomena, and improving the performance of catalytic systems.

Published on 15 fevral 2021. Downloaded by Cornell University Library on 21.04.2021 18:28:51.

Broader context

Advanced manufacturing as a method to create novel electrochemical reactors opens the door to many different energy technologies ahead. In combination with CO_2 electroreduction, excess renewable energy can effectively be stored as fuels and additives, as well as non-fossil derived consumer and industrial chemicals (*e.g.* monomers for polymerization and constructions materials) for longer-term sequestration of CO_2 out of environment. Reactor design and manufacturing is central to achieving progress toward these goals; understanding of the mass transport phenomena occurring within the reactor must be developed to build more efficient and effective systems. The high activity, selectivity, cathodic energy efficiency, CO_2 single-pass conversion and product yields achieved in this work were accomplished with a generic Cu catalyst in bulk neutral pH. This highlights the potential of this methodology in design optimization and enhanced system performance when sophisticated catalysts and/or reaction systems are employed. AM reactors represent a significant step towards de-risking scale-up and optimization of this game-changing technology while developing design metrics that can promote commercial feasibility. This work also validates that cost-effective AM techniques can be utilized for rapid production of modular system components with high precision and reproducibility that are necessary for future industrial deployment.

[a] *Materials Engineering Division, Lawrence Livermore National Laboratory, Livermore, CA 94550, USA. E-mail: duoss1@llnl.gov*
[b] *SUNCAT Center for Interface Science and Catalysis, Department of Chemical Engineering, Stanford University, Stanford, CA 94305, USA. E-mail: jaramillo@stanford.edu*
[c] *Materials Science Division, Lawrence Livermore National Laboratory, Livermore, CA 94550, USA. E-mail: baker74@llnl.gov, hahn31@llnl.gov*
[d] *Computational Engineering Division, Lawrence Livermore National Laboratory, Livermore, CA 94550, USA*
[e] *Total EP Research & Technology USA, LLC., Houston, TX 77002, USA*
[f] *SUNCAT Center for Interface Science and Catalysis, SLAC National Accelerator Laboratory, Menlo Park, CA 94025, USA*

† Electronic supplementary information (ESI) available. See DOI: 10.1039/d0ee03679j

‡ These authors contributed equally to this work.

Introduction

The accelerating need to mitigate global emissions of CO_2 has driven significant advancements in designing systems and strategies that transition towards a sustainable future.[1–3] However, a growing global population continues to rely on fossil-derived sources for power, chemicals, agriculture, and transportation sectors.[4] Converting this CO_2 to fuels and chemical feedstocks can be an effective way to reduce the CO_2 footprint of many conventional chemical processes, thus promoting a circular carbon-economy.[5] Considering the cheap (~$0.02 kW h^{-1}) and sometimes free renewable energy

Published on 15 fevral 2021. Downloaded by Cornell University Library on 21.04.2021 18:28:51.

generated in certain parts of the world, such energy can be stored by converting CO_2 to synthesis gas, future energy carriers (*e.g.* fuels and additives), and monomers for polymerization. Thus, electrochemical CO_2 reduction (CO_2R) to produce non-fossil sourced chemical products can be a significant milestone in decarbonizing the chemicals industry.

While there are several challenges associated with scaling up CO_2R, much progress has been made to better understand a variety of complex phenomena and coexisting processes. Aqueous-phase CO_2R, performed in liquid-fed reactors (LFRs) leveraging electrochemical[6–8] as well as photocatalytic[9,10] driving forces, served as the primary platform for investigating selectivity trends and discovering new materials.[11,12] Furthermore, studies in LFRs elucidated the effects of various intermediates, including *COOH,[8,13–15] *CO,[16,17] and even $*C_2O_4$[18] in light driven conditions, which aided in our understanding of reaction mechanisms. The transition from LFRs to vapor-fed reactors (VFRs) utilizing gas diffusion electrodes (GDEs) yielded higher performance metrics by minimizing the distance between the electrode and bulk vapor CO_2 stream.[19] Previous studies achieved high activity and selectivity towards the production of CO, $HCOO^-$, C_2H_4, and C_2H_5OH by capitalizing on the increased complexity and tunability of GDEs.[20] Despite recent advances, it is unclear whether the understanding of kinetic mechanisms and mass transport phenomena in LFRs translates to industrially relevant current densities observed in VFRs.

To date, published reports on electrochemical reactors for CO_2 reduction have all focused on components that rely on traditional manufacturing methods which are time- and resource intensive.[21,22] Industrial deployment of CO_2R technology to replace current production volumes of the chemical and petrochemical industry will require manufacturing millions of these system components with high precision and reproducibility for modular electrolyzers. Advanced manufacturing (AM) is a promising approach to overcome these limitations, as it allows for rapid prototyping and iteration of reactor components and parts with submicron control.[23,24] These advantages of AM have led to novel materials and devices for energy storage,[25] optics,[26] drug delivery,[27] and carbon capture applications.[28] However, there have been few studies to date that have employed AM for electrochemical reactor design,[29] and none to date for electrochemical CO_2 reduction.

For the first time to date, we demonstrate AM for fabrication of CO_2 electrolyzers with increased precision. This enables the rapid prototyping of different system components with conceptual design aspects and corresponding assessment of important design parameters. AM VFRs showcase promising results for CO_2 reduction with an unoptimized electrode, membrane, and electrolyte, including high selectivity for multi-carbon products at high current densities. We identify and evaluate mass transport regimes for various flow rate and electrochemical potential conditions and investigate underlying mass transport mechanisms. Consequently, we propose that for a given reactor and system configuration, the use of the dimensionless Damköhler (Da) number can elucidate regimes based on the proposed mechanisms. Lastly, we introduce yield as a key metric for evaluating performance of CO_2 electrolyzers.

Experimental methods

Reactor manufacturing and catalyst characterization

All experimental data was obtained from 3D-printed VFRs and components based on an informed and iterative reactor design process. Electrochemical reactors (Fig. S1, ESI†) and electrolyte sparging chambers were first drafted using computer-aided design (CAD) software (AutoCAD Inventor). Each VFR was designed with a 1.4 cm^2 geometric surface area for the cathode, anode, and membrane windows. As gas bubbles formed on the electrodes can influence mass transport and electric field uniformity within the reactor, compartments were designed with a tapered geometry to direct fluid flow for enhanced bubble management (Fig. S3, ESI†). All components were then printed using a stereolithography (SLA) 3D printer (FormLabs Form2, 25 μm step size); all components were made from a polyacrylate-based commercial resin (Formlabs). After printing, each reactor component was sonicated in an IPA bath for at least 30 minutes to remove any excess or uncured resin, then cured with UV light at 60 °C for 60 minutes. The components were then rinsed thoroughly in deionized water before use and rinsed thoroughly between experimental runs.

A 275 nm thick layer of Cu was deposited onto ePTFE (Sterlitech) using e-beam physical vapor deposition in a rotating chamber (see ESI† for full details). Scanning electron microscopy (SEM) images reveals the coating of Cu catalyst on top of the ePTFE fibers (Fig. S6, ESI†). X-ray photoelectron spectroscopy (XPS) validated both cleaned ePTFE and Cu/ePTFE samples (Fig. S7, ESI†). To identify the facets post-deposition, we performed X-ray diffraction (XRD) and observed Cu(111), Cu(200) and Cu(220) peaks (Fig. S8, ESI†). Double-layer capacitance was used to measure the electrochemically active surface area (ECSA) of the catalyst (Fig. S10, ESI†); the ECSA measured was similar to those measured other reports.[30–32]

Electrochemical experiments

All electrochemical experiments were carried out using a multichannel potentiostat (Bio-Logic). An IrO_2 catalyst on a carbon paper electrode (Dioxide Materials) was cut and used as the anode. A low-profile silver/silver chloride (Ag/AgCl) electrode (Pine Instruments) was used as the reference electrode and connected to the catholyte compartment of the reactor. A 50 μm Sustanion anion exchange membrane (Dioxide Materials) was inserted between the catholyte and anolyte chambers to mitigate the cross-over of impurities and products between the electrodes. Both catholyte and anolyte were recirculated using external 3D-printed chambers (each with a volume of 25 mL) to minimize local accumulation of products. Potentiostatic electrochemical impedance spectroscopy (PEIS) was used to measure the solution resistance (1) between the cathode and the reference electrode, and (2) between the cathode and the anode (Fig. S9, ESI†). Chronoamperometry (CA) was performed for 5 minutes at a soft overpotential of −0.75 V *vs.* Ag/AgCl to reduce any oxide on the Cu surface. Finally, chronopotentiometry (CP) was performed at a given current density; the solution resistance was measured every 3 minutes to allow

 This journal is © The Royal Society of Chemistry 2021

Published on 15 fevral 2021. Downloaded by Cornell University Library on 21.04.2021 18:28:51.

for correction of the voltage drop due to changes in electrolyte conductivity. The average resistance and potential from each run were used for analysis. Each experiment was duplicated to ensure each result was reproducible.

Results and discussion

We employed stereolithography 3D printing to develop several generations of vapor-fed electrochemical systems (Fig. 1a). Using AM instead of conventional manufacturing (CM), we reduced the cost and the amount of time to produce each reactor component by several orders of magnitude (Fig. 1b). Several metrics informed the rapid development from Generation 1 to Generation 3: the total cell resistance measured between the cathode and anode, the total cell potential to operate the reactor at 214 mA cm^{-2}, and the current density achieved at a compliance voltage of $\pm$10 V (Fig. 1c and d). Generation 1 reactors had a total cell resistance of 33.1 Ω, split between the electrolyte (22.3 Ω) and the membrane (10.7 Ω), which led to a large voltage drop ($\sim$10 V at 214 mA cm^{-2}) and a maximum current density of 266 mA cm^{-2}. Informed by these findings, Generation 2 reactors decreased the distance between the electrodes by over half, which consequently reduced the ohmic resistance. Accordingly, Generation 2 reactors exhibited a total cell resistance of 21.2 Ω, which represents a 34% decrease from Generation 1; however, the maximum current density achieved only increased to 297 mA cm^{-2}, indicating that ohmic resistance of the electrolyte was not the only limiting factor.

The Generation 3 system design connected the cathode gas and catholyte compartments in a 3D-printed sparging chamber, saturating the electrolyte with CO_2 and reducing pH gradients and concentration polarization (Fig. S2, ESI†). This also eliminated pressure differences between the gas compartments and the liquid compartments, minimizing breakthrough of electrolyte and flooding due to a pressure gradient. Additionally, Generation 3 reactors featured a fourth compartment for removal of oxygen and degassed carbon dioxide[33] from the anode at high current densities and maintained the same distance between the cathode and anode. With these changes to the reactor and system design, Generation 3 reactors achieved a lower cell resistance (17.7 Ω), which is primarily the result of a lower bulk pH due to continuous CO_2 saturation. At 214 mA cm^{-2}, Generation 3 reactors resulted in a $\sim$5 V drop due to ohmic losses, almost 50% less than that of Generation 1 reactors; this generation also exhibited higher faradaic efficiencies (FE) for ethylene and ethanol. This system reached current densities greater than 500 mA cm^{-2}, establishing the viability of AM for high-rate electrosynthesis from CO_2.

Evaluating performance of AM VFRs for various inlet CO_2 flow rates

Building upon the advancements of the Generation 3 reactor, we explored the CO_2R performance in depth for this AM system. We covered a range of CO_2 inlet flow rates of 5, 10, 20, and 40 sccm on a simple Cu/PTFE catalyst and in 1 M $KHCO_3$. For these conditions, we display the current density towards CO_2-reduced products (Fig. 2a) and the corresponding electrochemical CO_2 conversion (Fig. 2b). Peak conversion occurs for

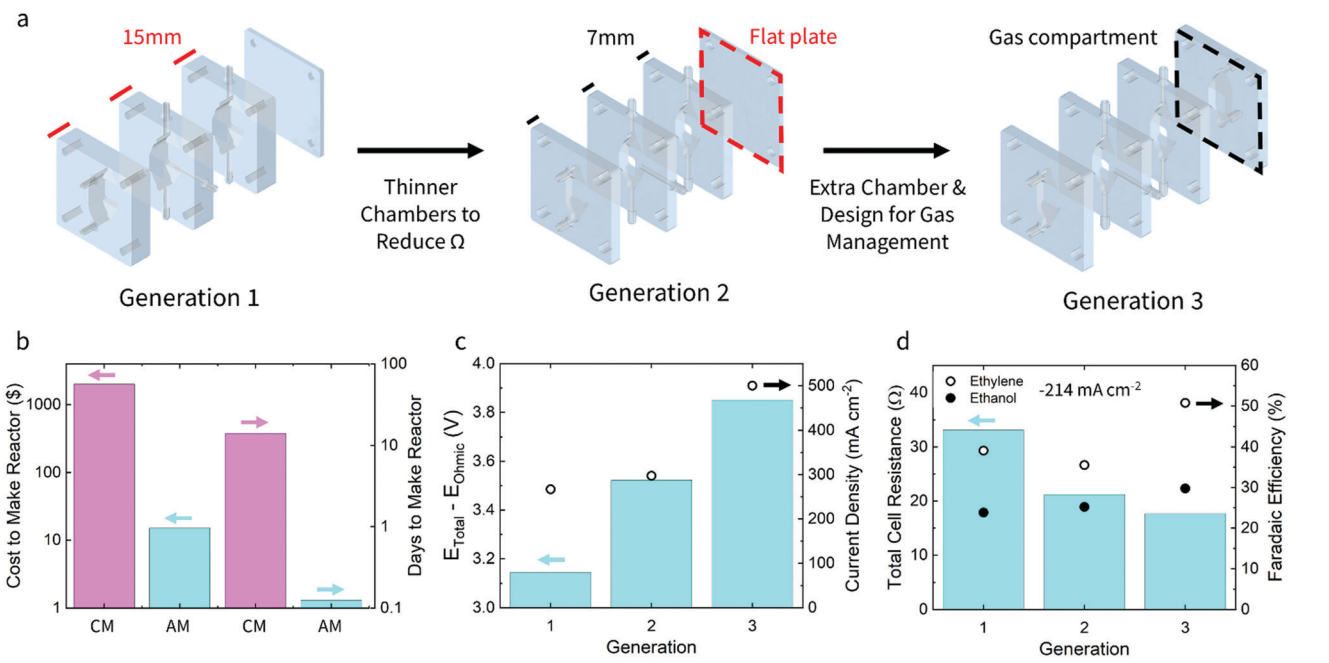

Fig. 1 Advantages of AM for electrochemical reactor design. (a) Schematic representation of three generations of reactors designed for CO_2R with brief description of changes between generations. (b) Order of magnitude advantages of AM over conventional manufacturing (CM) with regards to cost and time to produce electrolyzer. (c) Potential realized at electrodes (represented as the difference of the cell potential and the potential lost to ohmic drop) and maximum current density in each generation. (d) Total cell resistance and faradaic efficiencies of ethylene and ethanol at a fixed current density for all three generations.

Published on 15 fevral 2021. Downloaded by Cornell University Library on 21.04.2021 18:28:51.

all flow rate conditions at 357 mA cm^{-2}, with a maximum of 16.5% at 5 sccm. We observed two distinct regimes regarding CO_2 mass transport effects: an activation-controlled regime, which has sufficient transport of CO_2 for electroreduction, and a mixed-controlled regime, where both kinetic and mass transport effects lead to insufficient concentrations of CO_2 throughout catalyst layer.

We observe little to no effect of CO_2 flow rate on the activity and selectivity of products at lower current densities ($\leq$214 mA cm^{-2}), indicating this regime is activation controlled for all tested flow rates. At higher current densities, electrolytic performance differs with CO_2 flow rate, suggesting that some conditions operate in the mixed-controlled regime. At 357 mA cm^{-2}, the total CO_2R current ($\sim$235 mA cm^{-2}) at 5 sccm is lower than that of the other flow rates ($\sim$300 mA cm^{-2}). For >10 sccm, there is a positive correlation between ethylene production and CO_2 flow rate, while ethanol production remains unaffected, thus increasing the ratio of ethanol to ethylene (Fig. 2c). This trend is opposite of that observed in aqueous systems;[16] we attribute this to dramatic differences in the local environment and available CO_2 between VFRs and LFRs. The selectivity for ethylene at the catalyst surface could be influenced by the diffusion of the gaseous products into the PTFE and out with the effluent gas stream; this diffusion depends on the flow rate of CO_2 in the reactor. The diffusion of ethanol into the electrolyte is not sharply influenced by the CO_2 gas flow, suggesting the ethanol pathway is preferred when CO_2R is either partially or fully diffusion-controlled. Furthermore, the consistent activity towards ethanol may be influenced by the heterogeneity of active sites[34] and increased absorption of H on Cu.[35]

At 500 mA cm^{-2}, we observe a drop in CO_2R current density across flow rates <40 sccm; this is an extension of the effect seen at 5 sccm and 357 mA cm^{-2}. A decrease in ethylene production corresponds to an increase production of hydrogen and methane, accounting for the remainder of CO_2R current. At higher cathodic potentials, increased adsorption of hydrogen (*H) can suppress conversion of CO_2 to multi-carbon products.[17] Feeding CO_2 at 40 sccm resulted in reaching the mass transport limited current density previously observed at 357 mA cm^{-2}. This clear distinction between activation- and mixed-controlled regimes highlights the importance of both CO_2 inlet flow and applied current density on mass transport effects within electrochemical reactors.

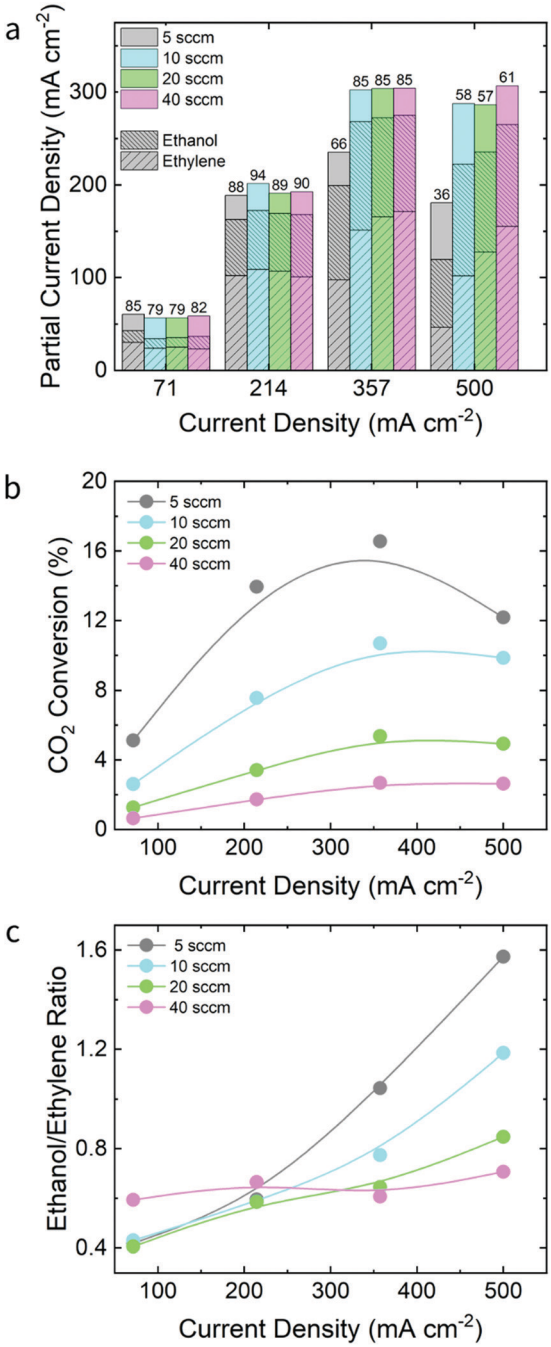

Fig. 2 (a) CO_2R partial current density as a function of total current density for various flow rates. Ethylene and ethanol fractions are shaded. Other CO_2R products (CO, $HCOO^-$, CH_4, CH_3COO^-, CH_3CHO, and C_3H_7OH) are grouped within the unshaded region. The CO_2R faradaic efficiency corresponding to condition is shown above each stacked column. (b) Electrochemical CO_2 conversion as a function of total current density for various flow rates. (c) Ratio of oxygenates to hydrocarbons as a function of flow rate and current density.

Mass transport limited current density in AM VFRs

We also investigated the effects of the electrode potential on electrocatalytic performance at 10 sccm CO_2 flow rates. The system demonstrated remarkable selectivity for CO_2R across a wide range of current densities (Fig. 3a), including over 90% FE for CO_2R from 142 mA cm^{-2} to 285 mA cm^{-2}; at 142 mA cm^{-2} we observed the maximum CO_2R cathodic energy efficiency and FE for the system at 49.6% (Fig. S15, ESI†) and 92.8% (Fig. S13, ESI†), respectively. Total C_{2+} FE reached a maximum of 85.9% FE at 214 mA cm^{-2}, which is one of the highest reported to multi-carbon products for CO_2R; the two major products formed were ethylene (50.7% at 214 mA cm^{-2}) and ethanol (33.9% at 357 mA cm^{-2}). Strikingly, we show here that high selectivity for CO_2R and CO_2 conversion can be achieved in bulk pH-neutral environments with no modifications or additives to either the catalyst or electrolyte. This compares favorably to previous reports using further-developed Cu electrodes and/or operating in alkaline conditions,[32,35–42] while mitigating issues associated with bulk electrolyte consumption of CO_2 that is

This journal is © The Royal Society of Chemistry 2021

Published on 15 fevral 2021. Downloaded by Cornell University Library on 21.04.2021 18:28:51.

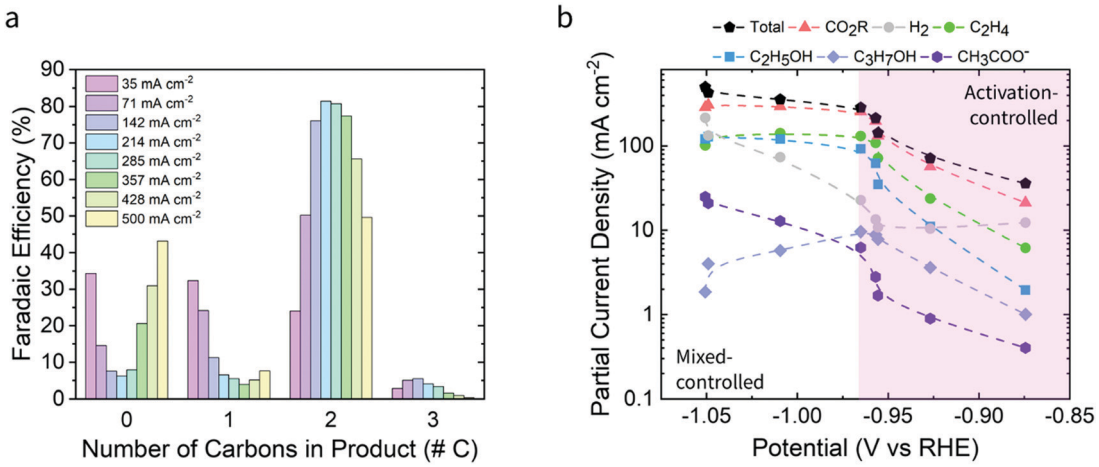

Fig. 3 (a) Selectivity towards 0-carbon (H_2), 1-carbon (CO, HCOO-, CH_4), 2-carbon (C_2H_4, C_2H_5OH, CH_3COO^-, CH_3CHO), and 3-carbon (C_3H_7OH) products at different current densities. (b) Partial current densities of select products and CO_2R, as well as total current density, as a function of applied cathodic potential.

particularly problematic in alkaline environments and can lead to lower overall system efficiency.[33]

Hydrogen, the only zero-carbon product, remained below 8% from 142 to 285 mA cm^{-2}, agreeing with previous reports depicting a preference for CO_2R within this current density range.[33,43] At current densities $\leq$285 mA cm^{-2}, hydrogen decreased in FE from 34% to 8% while 2-carbon products rapidly increased from 24% to 81%; formation of single-carbon products were consistently low in this regime. This inverse relationship is a result from several factors, including sufficient adsorption of *CO[17,43] and *COOH[8,13–15] intermediates on the catalyst surface and favorable kinetics for carbon–carbon coupling.[7,8,44] Furthermore, suppression of HER occurs *via* an increasing pH in the local environment;[32,33] we predict an increase up to 5 units for pH in our system (Fig. S21, ESI†).

Similar to the results from the flow rate study, we observed both activation-controlled and mixed-controlled regimes based on partial current densities and the corresponding electrochemical potential (Fig. 3b). The potential range from −0.87 V to −0.97 V *vs.* RHE corresponds to the activation-controlled regime; CO_2R current density increases exponentially as a function of potential, with product activities tracing the behavior of Butler–Volmer kinetics.[45] The partial current densities of the 2-carbon products (C_2H_4, C_2H_5OH, and CH_3COO^-) increase at similar rates in this regime; their slopes suggest the sharing of some reaction pathways and carbonaceous intermediates.[7,12,17,46]

A plateau in CO_2R current density of around ~300 mA cm^{-2} is a result of a transition from activation- to mixed-controlled regimes ($\leq$−0.97V *vs.* RHE). While ethylene and ethanol current densities reach an asymptote, H_2 and CH_4 partial current densities increase and agree with previous literature (Fig. S14, ESI†).[12,47,48] This relationship suggests a higher *H coverage on the catalyst surface, increasing the probability of protonating adsorbed single-carbon species. Interestingly, acetate partial current density increases throughout both regimes, suggesting acetate formation may correlate with concentration of OH^-.[49] As the total current density approaches 500 mA cm^{-2}, total CO_2 conversion decreases, suggesting a modified reaction environment that favors hydrogen evolution. At higher overpotentials, an high local pH and lower concentrations of $KHCO_3$ likely result in a dominant proton-donor shift to H_2O.[50] The CO_2 mass transport limitation observed in this region is analogous to results that have been observed in aqueous, liquid-fed CO_2R systems.[12]

CO_2 mass transport-limiting phenomena

There are several mass transport phenomena that control how CO_2 reaches the catalyst surface in aqueous electrolyte VFRs: diffusion of $CO_{2(g)}$ through the PTFE layer to the catalyst layer, dissolution of $CO_{2(g)}$ into the electrolyte to form $CO_{2(aq)}$, and diffusion of $CO_{2(aq)}$ to the catalyst surface. Many studies show that OH^- production at the cathode and consequent homogenous consumption of $CO_{2(aq)}$ to form carbonate can result in variable reactant concentrations, alter product selectivity, and limit CO_2 transport to the catalyst layer.[32,51–54] However, high current densities (>1 A cm^{-2}) to reduced products in alkaline conditions[40,42] suggest additional mass transport limiting phenomena must be present in these bulk neutral-media, AM VFR systems.

We propose that temperature can change the concentration of CO_2 at the gas–liquid interface, contributing to CO_2 mass transport limitations. While there is previous literature on the effect of temperature on CO_2R,[55–57] there remains a lack of experimental understanding on how temperature changes within VFRs during CO_2 electrolysis. We measured the temperature change of the catholyte near the cathode surface for both HER and CO_2R (Fig. 4). At current densities <300 mA cm^{-2}, the increase in temperature across the cathode is <7 °C for all experiments; this results from resistive heating of the electrolyte, as seen by the simulated temperature change from the model. As resistive heating is dependent on the applied current and electrolyte resistance, the measured increase in temperature for HER and CO_2R are similar in this range. At current densities

Published on 15 fevral 2021. Downloaded by Cornell University Library on 21.04.2021 18:28:51.

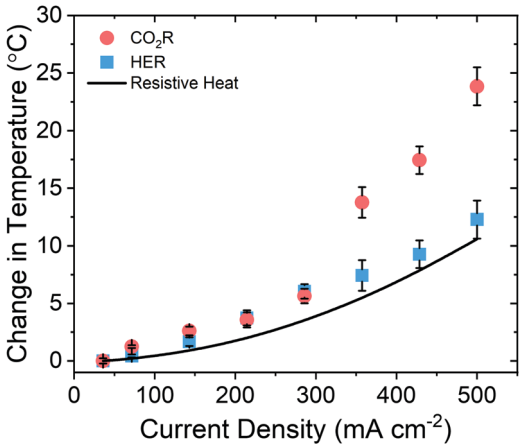

Fig. 4 Measured cathode temperature during electrolysis for CO_2R and HER at 10 sccm. Modeling of the expected increase in temperature based on resistive heating is represented as the solid black curve.

>300 mA cm^{-2}, the increase in temperature is higher in CO_2R (max of ~ 24 °C at 500 mA cm^{-2}) than in HER (max of ~ 12 °C at 500 mA cm^{-2}). The exothermic reaction of OH^- with CO_2 and the heats of reaction from all electrochemical reactions at the catalyst surface contribute significantly to the difference in temperature increase.

Dynamic changes in temperature change several key variables that can impact CO_2 mass transport. At higher temperatures, the solubility of CO_2 decreases from 33.4 mM at 25 °C to 21.0 mM at 45 °C. Coupled with higher concentrations of OH^- in the electrolyte, this can reduce the amount of CO_2 that is available to the catalyst, leading to a mass transport limited current density for CO_2R. Additionally, temperature increases can change the conductivity of the electrolyte and the diffusion of various species in the aqueous phase; it can also influence the kinetic barriers for CO_2R reaction pathways, which can alter the selectivity of the catalyst and limit the rate of CO_2R at high current densities.

Additionally, we hypothesize that changes in wettability of the PTFE support can contribute to CO_2 mass transport limitations.[58] Solvent water does not wet the PTFE support and the triple phase interface remains abrupt and close to the cathode.[32] Liquid products (particularly ethanol) that are produced in the catalyst layer can wet the PTFE support by changing the solvent surface tension.[58] Based on contact angle measurements (Fig. 5a), only a small concentration of $\sim 2\%$ (by mass) of ethanol is sufficient to change the hydrophobicity of the PTFE from non-wetting ($\Theta > 105^\circ$) to neutrally wetting ($75^\circ < \Theta < 105^\circ$).[59] We calculate a maximum ethanol concentration of $>3.5\%$ for a range of current densities in our reactor (Fig. 5b); this suggests that the electrolyte could begin penetrating the neutrally wet PTFE interface. Electrolyte penetrating the PTFE could block pores and extend the gas-electrolyte interface, inhibiting CO_2 mass transfer.[51,58] It is challenging to determine the exact depth of electrolyte penetration due to species transport, local pressure, capillary forces, and the specific geometry of PTFE fibers.

Insights from dimensionless number analysis

We sought to use a single parameter that incorporates the aforementioned mass transport mechanisms (Scheme 1) to better understand operating regimes. The Damköhler number, Da, is a dimensionless quantity that represents the ratio between diffusion and reaction time scales. We define Da to solicit a regime diagram for transport within the GDE (eqn (1)):

$$\mathrm{Da}_{\mathrm{diff}} = \frac{\tau_{\mathrm{DMI}}}{[\mathrm{CO}_{2,0}]P/m} = \frac{\nu P}{[\mathrm{CO}_{2,0}]D_{\mathrm{CO}_2}} \quad (1)$$

where m represents the molar consumption per unit area from reduction ($m = j/nF$, where j is the current density), and P is the liquid penetration depth into the ePTFE. We performed a timescale analysis representing diffusion of CO_2 to decouple activation- and mixed-controlled regimes. When the timescale for CO_2 diffusion to the catalyst layer is greater than the timescale for surface reactions, we define the system to be

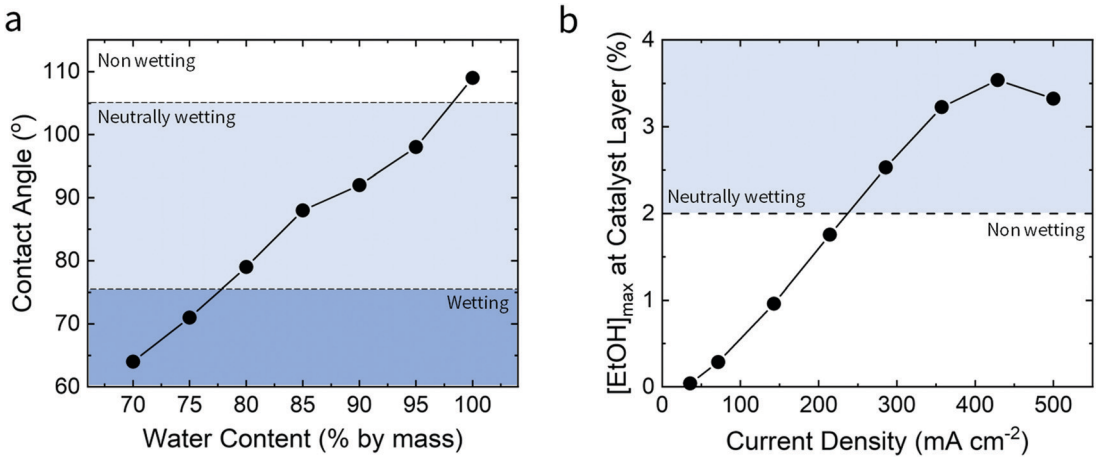

Fig. 5 (a) Contact angle measurements for ethanol/water mixtures on bulk PTFE. This represents a conservative estimate for wetting of electrodes, as the Cu catalyst is more hydrophilic than PFTE. (b) Calculated maximum ethanol concentrations at the gas–liquid–solid interface as a function of total current density. Shaded and unshaded zone represents neutrally wetted and non-wetted regions, respectively.

 This journal is © The Royal Society of Chemistry 2021

Published on 15 fevral 2021. Downloaded by Cornell University Library on 21.04.2021 18:28:51.

operating in a CO_2 mass transport limited regime (Da > 1). As higher current densities are reached, the combination of mass transport limiting mechanisms can push the system towards the Da > 1 regime.

Contour plots (Fig. 6) elucidate different mass transport regimes based on CO_2 gas–liquid interface concentrations of 33 (25 °C) and 21 mM (45 °C). For a system operating ≥100 mA cm^{-2} with an interfacial CO_2 concentration of 33 mM (Fig. 6a), we predict that ≤5 μm of electrolyte penetration will push the system towards a Da > 1 regime. As current density increases, this effect is exacerbated due to increased OH^- generation. When extending this to lower interfacial CO_2 concentrations, we see the quantity of penetration to induce mass transport limitations is further decreased. At 21 mM – a concentration corresponding to the temperature measurements during electrolysis – the system enters the mass transport limited regime at ≤2 μm penetration at ≥100 mA cm^{-2} (Fig. 6b).

This model provides the framework for using Da as a relevant dimensionless number to distinguish when a VFR is CO_2 mass transport limited for any reactor and system design. Other additional variables, including the contributions from catalyst deformation, are not accounted in this model; however, those effects are less likely to lead to our observations. Using Da to understand the primary drivers and bottlenecks for species transport can lead to better design and operation of reactors to overcome these limitations. Furthermore, AM presents a promising platform for coupling with computational fluid dynamics for greater understanding of these electrochemical systems.

Achieving high yield of ethanol and ethylene in AMVFRs

When assessing the feasibility of these systems, optimization of operating conditions and system components toward specific products has seen significant advancements. However, this does not account for the flowrate of CO_2 into the cathodic gas compartment; maximizing product formation per molecule of CO_2 is imperative for improving the economic viability of CO_2 electrolysis. This ratio, known as yield, is defined for an CO_2R process below:

$$\text{Yield} = \frac{\text{products out}}{\text{reactants in}} = \frac{\text{mol } C_xH_yO_z \text{ produced}}{\text{mol } CO_2 \text{ in}} \quad (2)$$

Product yield is critical as a primary metric to evaluate the reactor performance in many industries. Considering the differences in catalyst composition and reaction area, local electrolyte environment, and reactor and system design, we employ it here as a quantitative metric that can be used to compare results from many reports across the field.

We compare the ethylene (Fig. 7a) and ethanol (Fig. 7b) yield for the highest performing set of conditions from various reports. We classify the results from literature into three categories for the electrolyte environment (neutral pH, alkaline pH, and membrane electrode assembly or MEA) and three categories for the catalyst composition (Cu/CuO_x, Cu/additive, and bimetallics). The AM VFRs in this work achieve high yield towards ethylene (3.67%), which is amongst the highest performing systems for neutral electrolytes in literature (Fig. 7a). As expected, there is an inverse relationship between product yield and CO_2 flow rate (Fig. S30, ESI†).

On a partial current density basis, ethanol production is limited by challenging kinetics and a focus on conditions that favor the competing ethylene pathway.[32,40,65] While various reports have shown improved selectivity toward ethanol,[35,39,41] these findings are attributed to advanced catalyst formulation and/or tuning of electrolyte and environment. With consistent

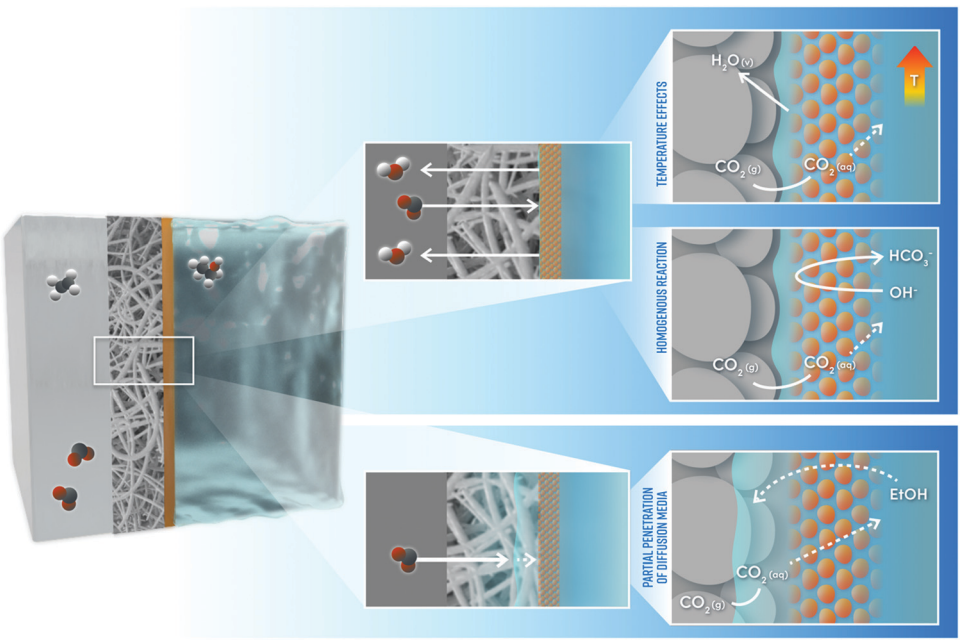

Scheme 1 Proposed phenomena that can impact CO_2 mass transport to the catalyst surface: temperature effects, homogenous reaction, and partial penetration into diffusion media.

Published on 15 fevral 2021. Downloaded by Cornell University Library on 21.04.2021 18:28:51.

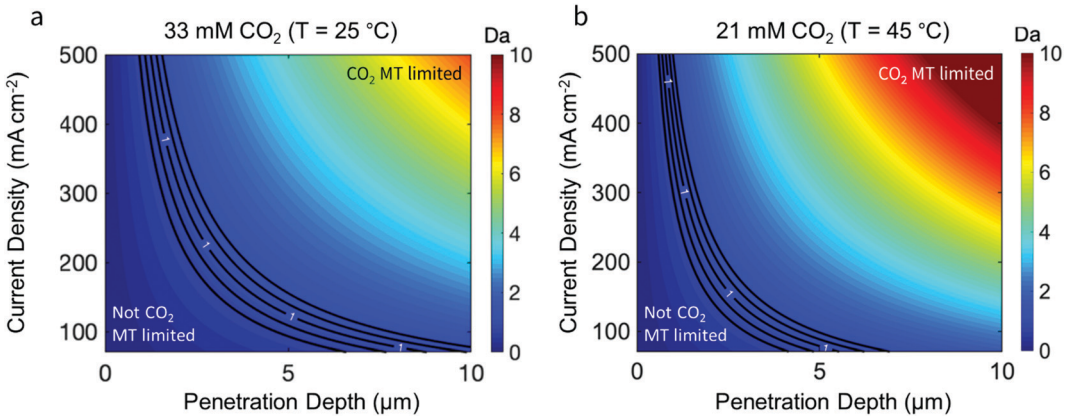

Fig. 6 Contour plots of Da, with contour lines at near the mass transport limitation boundary of Da ~ 1 (Da = 0.75–1.25), representing two conditions for CO_2 concentration at the gas–liquid interface corresponding to (a) 33 mM (25 °C) and (b) 21 mM (45 °C).

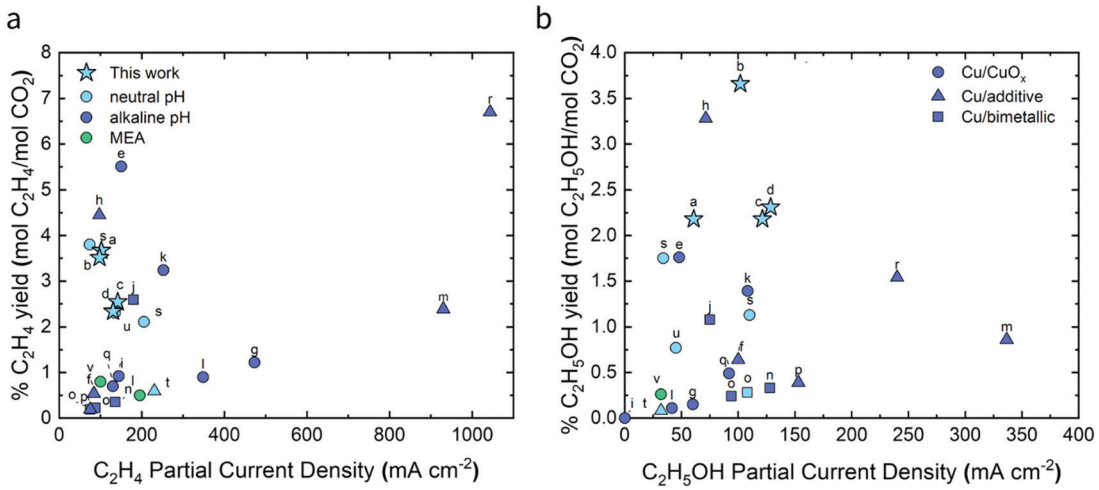

Fig. 7 Comparison of literature and this work for (a) % ethylene and (b) % ethanol yield as a function of partial current density. Indigo colored data represents VFRs with bulk alkaline pH including [e] Ma *et al.*;[36] [f] Zhuang *et al.*;[60] [g] Dinh *et al.*;[32] [h] Hoang *et al.*;[61] [i] Wang *et al.*;[37] [j] Hoang *et al.*;[38] [k] Lv *et al.*;[39] [l] Wang *et al.*;[62] [m] Arquer *et al.*;[40] [n] Luo *et al.*;[35] [o] Li *et al.*;[63] [p] Wang *et al.*;[41] [q] Yang *et al.*;[64] [r] Ma *et al.*[42] Light blue colored data represents VFRs with bulk neutral pH including [a–d] this work; [o] Li *et al.*;[63] [s] Tan *et al.*;[43] [t] Li *et al.*;[65] [u] Ma *et al.*[33] Green colored data represents MEA VFRs including [l] Wang *et al.*;[62] [v] Garbardo *et al.*[66] Point shapes represent catalyst layer composition class: Cu/Cu_x, Cu modified with a non-metal additive, and Cu-based bimetallics.

production of ethanol in AMVFRs across a range of CO_2 flow rates, we report the highest yield to date towards ethanol (3.66%). This work affirms that high yield towards multi-carbon products from CO_2 can be achieved with generic Cu catalysts in moderate electrolyte conditions.

Conclusions

In this work, we introduce a new paradigm for chemical production using advanced manufacturing. We highlight prospects of AM for accelerated improvement and development of CO_2 electrolyzers *via* reactor design; using 3D printing instead of conventional machining can lead to significant improvements in activity, selectivity, yield, and energy efficiency through rapid iteration. We realize reactor design, in addition to electrode and electrolyte engineering, as a key variable for CO_2 reduction. Insights gained from this work can be employed for all vapor-fed reactors to improve performance and build understanding.

The potential of this design strategy can lead to well-characterized and scalable systems, especially when coupled with computational efforts and technoeconomic analyses. Furthermore, we anticipate the implementation of AM for deterministic electrode, catalyst and membrane development. This work demonstrates, for the first time, AM as a platform for creating robust vapor-fed reactors and components for high-performance CO_2 reduction. We are optimistic that AM will transform our approach towards designing systems for catalysis and propel the design of novel reactors for the next generation of chemicals synthesis.

 This journal is © The Royal Society of Chemistry 2021

Published on 15 fevral 2021. Downloaded by Cornell University Library on 21.04.2021 18:28:51.

Author contributions

D. C. and J. T. F. contributed significantly and equally to this work. Writing – original draft: D. C. and J. D. C. and J. T. F. contributed significantly and equally to this work. Writing – Original Draft: D. C., J. T. F., S. S., J. D., D. L., and A. A. W.; Writing – Review & Editing: D. C., J. T. F., S. S., J. D., D. L., A. A. W., A. S., C. H., T. F. J., S. B., and E. D.; Conceptualization: J. T. F., D. C., S. S., J. D., D. L., A. A. W., V. A. B., C. H., T. F. J., S. B., and E. D.; Investigation: D. C., J. T. F., S. S., J. D., D. L., A. A. W., and J. H.; Methodology: J. T. F., D. C., S. S., J. D., J. H. and V. A. B.; Formal Analysis: S. S., J. D., and V. A. B.; Software: V. A. B., S. S., J. D.; Validation: D. C., J. T. F., S. S., J. D., D. L., A. A. W., J. H., and V. A. B.; Project Administration: J. T. F., D. C., V. A. B., C. H., T. F. J., S. B., and E. D.; Funding Acquisition: A. S., C. H., T. F. J., S. B., and E. D.

Conflicts of interest

The authors declare no competing interests.

Acknowledgements

This work was performed under the auspices of the U.S. Department of Energy by Lawrence Livermore National Laboratory under Contract DE-AC52-07NA27344 and was supported by Laboratory Directed Research and Development funding under project 19-SI-005 and a cooperative research and development agreement among Lawrence Livermore National Laboratory, Stanford University and TOTAL American Services, Inc. (affiliate of TOTAL SE) under agreement number TC02307, which also supported research efforts at Stanford and SLAC National Accelerator Laboratory. Daniel Corral thanks the GEM Fellowship at Stanford University and Lawrence Livermore National Laboratory, as well as the Stanford Graduate Fellowship. The authors thank Veronica Chen and the TID Team at Lawrence Livermore National Laboratory for preparation of the TOC figure and Scheme 1. The authors thank and appreciate guidance from colleagues at Lawrence Livermore National Laboratory, including Dr April Sawvel, Hannah Eshelman, Cameron Cornell, Dr Zhen Qi, Dr Nikola Dudukovic, Dr Thomas Moore, Dr Jon Lee, Dr Jonathan Davis, Dr Felicia Lucci, Dr Marcus Worsley, Tony Baylis, and Dr Roger Aines. The authors thank and appreciate guidance from colleagues at Stanford University, including Dr David Wakerley, Dr Sarah Lamaison, and Dr Lei Wang. The authors thank Dr Shaffiq Jaffer, Prof. Edward Sargent, Prof. David Sinton, and members of the Sargent Group and Sinton Group at the University of Toronto for helpful discussions. The authors thank the Nuclear Magnetic Resonance Spectroscopy and Cleanroom Facilities at Lawrence Livermore National Laboratory, the Stanford Nano-Shared Facilities at Stanford University, and the Contact Angle Facilities at SLAC National Laboratory.

References

1 B. Obama, The irreversible momentum of clean energy, *Science*, 2017, **355**, 126–129.
2 Intergovernmental Panel on Climate Change (2014). Clim. Change 2014 Synth. Rep.
3 S. Chu, Y. Cui and N. Liu, The path towards sustainable energy, *Nat. Mater.*, 2017, **16**, 16.
4 International Energy Outlook 2019 (2019).
5 P. De Luna, C. Hahn, D. Higgins, S. A. Jaffer, T. F. Jaramillo and E. H. Sargent, What would it take for renewably powered electrosynthesis to displace petrochemical processes?, *Science*, 2019, **364**, eaav3506.
6 Y. Hori, H. Wakebe, T. Tsukamoto and O. Koga, Electrocatalytic process of CO selectivity in electrochemical reduction of CO_2 at metal electrodes in aqueous media, *Electrochim. Acta*, 1994, **39**, 1833–1839.
7 K. P. Kuhl, E. R. Cave, D. N. Abram and T. F. Jaramillo, New insights into the electrochemical reduction of carbon dioxide on metallic copper surfaces, *Energy Environ. Sci.*, 2012, **5**, 7050.
8 A. A. Peterson, F. Abild-Pedersen, F. Studt, J. Rossmeisl and J. K. Nørskov, How copper catalyzes the electroreduction of carbon dioxide into hydrocarbon fuels, *Energy Environ. Sci.*, 2010, **3**, 1311–1315.
9 M. Zhang, J. Cheng, X. Xuan, J. Zhou and K. Cen, Pt/graphene aerogel deposited in Cu foam as a 3D binder-free cathode for CO_2 reduction into liquid chemicals in a TiO_2 photoanode-driven photoelectrochemical cell, *Chem. Eng. J.*, 2017, **322**, 22–32.
10 M. Zhang, X. Xuan, W. Wang, C. Ma and Z. Lin, Anode Photovoltage Compensation-Enabled Synergistic CO_2 Photoelectrocatalytic Reduction on a Flower-Like Graphene-Decorated Cu Foam Cathode, *Adv. Funct. Mater.*, 2020, **30**, 2005983.
11 J. Resasco and A. T. Bell, Electrocatalytic CO_2 Reduction to Fuels: Progress and Opportunities, *Trends Chem.*, 2020, **2**, 825–836.
12 S. Nitopi, E. Bertheussen, S. B. Scott, X. Liu, A. K. Engstfeld, S. Horch, B. Seger, I. E. L. Stephens, K. Chan and C. Hahn, *et al.*, Progress and Perspectives of Electrochemical CO_2 Reduction on Copper in Aqueous Electrolyte, *Chem. Rev.*, 2019, **119**, 7610–7672.
13 H. Yang, Y. Hu, J. Chen, M.-S. Balogun, T. Jie, P. Fang, S. Zhang, J. Chen and Y. Tong, Intermediates Adsorption Engineering of CO_2 Electroreduction Reaction in Highly Selective Heterostructure Cu-Based Electrocatalysts for CO Production, *Adv. Energy Mater.*, 2019, **9**, 1901396.
14 J. T. Feaster, C. Shi, E. R. Cave, T. Hatsukade, D. N. Abram, K. P. Kuhl, C. Hahn, J. K. Nørskov and T. F. Jaramillo, Understanding selectivity for the electrochemical reduction of carbon dioxide to formic acid and carbon monoxide on metal electrodes, *ACS Catal.*, 2017, **7**, 4822–4827.
15 G. Neri, J. J. Walsh, G. Teobaldi, P. M. Donaldson and A. J. Cowan, Detection of catalytic intermediates at an electrode surface during carbon dioxide reduction by an earth-abundant catalyst, *Nat. Catal.*, 2018, 1.

Published on 15 fevral 2021. Downloaded by Cornell University Library on 21.04.2021 18:28:51.

16 C. Hahn, T. Hatsukade, Y.-G. Kim, A. Vailionis, J. H. Baricuatro, D. C. Higgins, S. A. Nitopi, M. P. Soriaga and T. F. Jaramillo, Engineering Cu surfaces for the electrocatalytic conversion of CO_2: Controlling selectivity toward oxygenates and hydrocarbons, *Proc. Natl. Acad. Sci. U. S. A.*, 2017, **114**, 5918–5923.

17 X. Liu, P. Schlexer, J. Xiao, Y. Ji, L. Wang, R. B. Sandberg, M. Tang, K. S. Brown, H. Peng and S. Ringe, *et al.*, pH effects on the electrochemical reduction of CO (2) towards C 2 products on stepped copper, *Nat. Commun.*, 2019, **10**, 32.

18 H. Sheng, M. H. Oh, W. T. Osowiecki, W. Kim, A. P. Alivisatos and H. Frei, Carbon Dioxide Dimer Radical Anion as Surface Intermediate of Photoinduced CO_2 Reduction at Aqueous Cu and CdSe Nanoparticle Catalysts by Rapid-Scan FT-IR Spectroscopy, *J. Am. Chem. Soc.*, 2018, **140**, 4363–4371.

19 R. Mauri, *Transport phenomena in multiphase flows*, Springer, 2015.

20 D. Higgins, C. Hahn, C. Xiang, T. F. Jaramillo and A. Z. Weber, Gas-Diffusion Electrodes for Carbon Dioxide Reduction: A New Paradigm, *ACS Energy Lett.*, 2019, **4**, 317–324.

21 S. Liang, N. Altaf, L. Huang, Y. Gao and Q. Wang, Electrolytic cell design for electrochemical CO_2 reduction, *J. CO_2 Util.*, 2020, **35**, 90–105.

22 J.-B. Vennekoetter, R. Sengpiel and M. Wessling, Beyond the catalyst: How electrode and reactor design determine the product spectrum during electrochemical CO_2 reduction, *Chem. Eng. J.*, 2019, **364**, 89–101.

23 I. Gibson, D. Rosen and B. Stucker, *Additive Manufacturing Technologies*, 2010, p. 238.

24 E. B. Duoss, T. H. Weisgraber, K. Hearon, C. Zhu, W. Small IV, T. R. Metz, J. J. Vericella, H. D. Barth, J. D. Kuntz and R. S. Maxwell, *et al.*, Three-dimensional printing of elastomeric, cellular architectures with negative stiffness, *Adv. Funct. Mater.*, 2014, **24**, 4905–4913.

25 C. Zhu, T. Liu, F. Qian, W. Chen, S. Chandrasekaran, B. Yao, Y. Song, E. B. Duoss, J. D. Kuntz and C. M. Spadaccini, *et al.*, 3D printed functional nanomaterials for electrochemical energy storage, *Nano Today*, 2017, **15**, 107–120.

26 D. T. Nguyen, C. Meyers, T. D. Yee, N. A. Dudukovic, J. F. Destino, C. Zhu, E. B. Duoss, T. F. Baumann, T. Suratwala and J. E. Smay, *et al.*, 3D-printed transparent glass, *Adv. Mater.*, 2017, **29**, 1701181.

27 E. A. Clark, M. R. Alexander, D. J. Irvine, C. J. Roberts, M. J. Wallace, J. Yoo and R. D. Wildman, Making tablets for delivery of poorly soluble drugs using photoinitiated 3D inkjet printing, *Int. J. Pharm.*, 2020, **578**, 118805.

28 J. J. Vericella, S. E. Baker, J. K. Stolaroff, E. B. Duoss, J. O. Hardin, J. Lewicki, E. Glogowski, W. C. Floyd, C. A. Valdez and W. L. Smith, *et al.*, Encapsulated liquid sorbents for carbon dioxide capture, *Nat. Commun.*, 2015, **6**, 1–7.

29 J. C. Bui, J. T. Davis and D. V. Esposito, 3D-Printed electrodes for membraneless water electrolysis, *Sustainable Energy Fuels*, 2020, **4**, 213–225.

30 K. Yang, R. Kas, W. A. Smith and T. Burdyny, Role of the Carbon-Based Gas Diffusion Layer on Flooding in a Gas Diffusion Electrode Cell for Electrochemical CO_2 Reduction, *ACS Energy Lett.*, 2021, **6**, 33–40.

31 J. Zhang, W. Luo and A. Züttel, Self-supported copper-based gas diffusion electrodes for CO_2 electrochemical reduction, *J. Mater. Chem. A*, 2019, **7**, 26285–26292.

32 C.-T. Dinh, T. Burdyny, M. G. Kibria, A. Seifitokaldani, C. M. Gabardo, F. P. G. de Arquer, A. Kiani, J. P. Edwards, P. De Luna and O. S. Bushuyev, *et al.*, CO_2 electroreduction to ethylene via hydroxide-mediated copper catalysis at an abrupt interface, *Science*, 2018, **360**, 783–787.

33 M. Ma, E. L. Clark, K. T. Therkildsen, S. Dalsgaard, I. Chorkendorff and B. Seger, Insights into the carbon balance for CO_2 electroreduction on Cu using gas diffusion electrode reactor designs, *Energy Environ. Sci.*, 2020, **13**, 977–985.

34 L. Wang, S. A. Nitopi, E. Bertheussen, M. Orazov, C. G. Morales-Guio, X. Liu, D. C. Higgins, K. Chan, J. K. Nørskov and C. Hahn, *et al.*, Electrochemical Carbon Monoxide Reduction on Polycrystalline Copper: Effects of Potential, Pressure, and pH on Selectivity toward Multicarbon and Oxygenated Products, *ACS Catal.*, 2018, **8**, 7445–7454.

35 M. Luo, Z. Wang, Y. C. Li, J. Li, F. Li, Y. Lum, D.-H. Nam, B. Chen, J. Wicks and A. Xu, *et al.*, Hydroxide promotes carbon dioxide electroreduction to ethanol on copper via tuning of adsorbed hydrogen, *Nat. Commun.*, 2019, **10**, 1–7.

36 S. Ma, M. Sadakiyo, R. Luo, M. Heima, M. Yamauchi and P. J. Kenis, One-step electrosynthesis of ethylene and ethanol from CO_2 in an alkaline electrolyzer, *J. Power Sources*, 2016, **301**, 219–228.

37 Y. Wang, H. Shen, K. J. Livi, D. Raciti, H. Zong, J. Gregg, M. Onadeko, Y. Wan, A. Watson and C. Wang, Copper Nanocubes for CO_2 Reduction in Gas Diffusion Electrodes, *Nano Lett.*, 2019, **19**, 8461–8468.

38 T. T. Hoang, S. Verma, S. Ma, T. T. Fister, J. Timoshenko, A. I. Frenkel, P. J. Kenis and A. A. Gewirth, Nanoporous Copper–Silver Alloys by Additive-Controlled Electrodeposition for the Selective Electroreduction of CO_2 to Ethylene and Ethanol, *J. Am. Chem. Soc.*, 2018, **140**, 5791–5797.

39 J.-J. Lv, M. Jouny, W. Luc, W. Zhu, J.-J. Zhu and F. Jiao, A highly porous copper electrocatalyst for carbon dioxide reduction, *Adv. Mater.*, 2018, **30**, 1803111.

40 F. P. G. de Arquer, C.-T. Dinh, A. Ozden, J. Wicks, C. McCallum, A. R. Kirmani, D.-H. Nam, C. Gabardo, A. Seifitokaldani and X. Wang, *et al.*, CO_2 electrolysis to multicarbon products at activities greater than 1 A cm- 2, *Science*, 2020, **367**, 661–666.

41 X. Wang, Z. Wang, F. P. García de Arquer, C.-T. Dinh, A. Ozden, Y. C. Li, D.-H. Nam, J. Li, Y.-S. Liu and J. Wicks, *et al.*, Efficient electrically powered CO_2-to-ethanol *via* suppression of deoxygenation, *Nat. Energy*, 2020, **5**, 478–486.

42 W. Ma, S. Xie, T. Liu, Q. Fan, J. Ye, F. Sun, Z. Jiang, Q. Zhang, J. Cheng and Y. Wang, Electrocatalytic reduction of CO_2 to ethylene and ethanol through hydrogen-assisted C–C

 This journal is © The Royal Society of Chemistry 2021

Published on 15 fevral 2021. Downloaded by Cornell University Library on 21.04.2021 18:28:51.

coupling over fluorine-modified copper, *Nat. Catal.*, 2020, **3**, 478–487.

43 Y. C. Tan, K. B. Lee, H. Song and J. Oh, Modulating Local CO_2 Concentration as a General Strategy for Enhancing C–C Coupling in CO_2 Electroreduction, *Joule*, 2020, **4**, 1104–1120.

44 W. Luo, X. Nie, M. J. Janik and A. Asthagiri, Facet Dependence of CO_2 Reduction Paths on Cu Electrodes, *ACS Catal.*, 2016, **6**, 219–229.

45 V. S. Bagotsky, *Fundamentals of Electrochemistry*, John Wiley & Sons, 2005.

46 Y. Lum, T. Cheng, W. A. Goddard and J. W. Ager, Electrochemical CO Reduction Builds Solvent Water into Oxygenate Products, *J. Am. Chem. Soc.*, 2018, **140**, 9337–9340.

47 K. P. Kuhl, T. Hatsukade, E. R. Cave, D. N. Abram, J. Kibsgaard and T. F. Jaramillo, Electrocatalytic Conversion of Carbon Dioxide to Methane and Methanol on Transition Metal Surfaces, *J. Am. Chem. Soc.*, 2014, **136**, 14107–14113.

48 X. Wang, A. Xu, F. Li, S.-F. Hung, D.-H. Nam, C. M. Gabardo, Z. Wang, Y. Xu, A. Ozden and A. S. Rasouli, *et al.*, Efficient methane electrosynthesis enabled by tuning local CO_2 availability, *J. Am. Chem. Soc.*, 2020, **142**, 3525–3531.

49 W. Luc, X. Fu, J. Shi, J.-J. Lv, M. Jouny, B. H. Ko, Y. Xu, Q. Tu, X. Hu and J. Wu, *et al.*, Two-dimensional copper nanosheets for electrochemical reduction of carbon monoxide to acetate, *Nat. Catal.*, 2019, **2**, 423–430.

50 J. Resasco, Y. Lum, E. Clark, J. Z. Zeledon and A. T. Bell, Effects of anion identity and concentration on electrochemical reduction of CO_2, *ChemElectroChem*, 2018, **5**, 1064–1072.

51 L.-C. Weng, A. T. Bell and A. Z. Weber, Modeling gas-diffusion electrodes for CO_2 reduction, *Phys. Chem. Chem. Phys.*, 2018, **20**, 16973–16984.

52 K. Wu, E. Birgersson, B. Kim, P. J. A. Kenis and I. A. Karimi, Modeling and Experimental Validation of Electrochemical Reduction of CO_2 to CO in a Microfluidic Cell, *J. Electrochem. Soc.*, 2014, **162**, F23.

53 C. Delacourt and J. Newman, Mathematical Modeling of CO_2 Reduction to CO in Aqueous Electrolytes: II. Study of an Electrolysis Cell Making Syngas from and Reduction at Room Temperature, *J. Electrochem. Soc.*, 2010, **157**, B1911.

54 R. Kas, K. Yang, D. Bohra, R. Kortlever, T. Burdyny and W. A. Smith, Electrochemical CO_2 reduction on nanostructured metal electrodes: fact or defect?, *Chem. Sci.*, 2020, **11**, 1738–1749.

55 Y. Zong, P. Chakthranont and J. Suntivich, Temperature Effect of CO_2 Reduction Electrocatalysis on Copper: Potential Dependency of Activation Energy, *J. Electrochem. Energy Convers. Storage*, 2020, **17**, 041007.

56 P. Lobaccaro, M. R. Singh, E. L. Clark, Y. Kwon, A. T. Bell and J. W. Ager, Effects of temperature and gas–liquid mass transfer on the operation of small electrochemical cells for the quantitative evaluation of CO_2 reduction electrocatalysts, *Phys. Chem. Chem. Phys.*, 2016, **18**, 26777–26785.

57 L.-C. Weng, A. T. Bell and A. Z. Weber, Towards membrane-electrode assembly systems for CO_2 reduction: a modeling study, *Energy Environ. Sci.*, 2019, **12**, 1950–1968.

58 M. E. Leonard, M. Orella, N. Aiello, Y. Roman-Leshkov, A. Forner-Cuenca and F. Brushett, Editors' Choice---Flooded by Success: On the Role of Electrode Wettability in CO_2 Electrolyzers that Generate Liquid Products, *J. Electrochem. Soc.*, 2020, **167**, 124521.

59 J. Guancheng, *Concept of Gas Wettability and Research Status. In Gas Wettability of Reservoir Rock Surfaces with Porous Media*, ed. J. Guancheng, Gulf Professional Publishing, 2018, ch. 1, pp. 1–27.

60 T.-T. Zhuang, Z.-Q. Liang, A. Seifitokaldani, Y. Li, P. De Luna, T. Burdyny, F. Che, F. Meng, Y. Min and R. Quintero-Bermudez, *et al.*, Steering post-C–C coupling selectivity enables high efficiency electroreduction of carbon dioxide to multi-carbon alcohols, *Nat. Catal.*, 2018, **1**, 421–428.

61 T. T. Hoang, S. Ma, J. I. Gold, P. J. Kenis and A. A. Gewirth, Nanoporous copper films by additive-controlled electrodeposition: CO_2 reduction catalysis, *ACS Catal.*, 2017, **7**, 3313–3321.

62 Y. Wang, Z. Wang, C.-T. Dinh, J. Li, A. Ozden, M. G. Kibria, A. Seifitokaldani, C.-S. Tan, C. M. Gabardo and M. Luo, *et al.*, Catalyst synthesis under CO_2 electroreduction favours faceting and promotes renewable fuels electrosynthesis, *Nat. Catal.*, 2020, **3**, 98–106.

63 Y. C. Li, Z. Wang, T. Yuan, D.-H. Nam, M. Luo, J. Wicks, B. Chen, J. Li, F. Li and F. P. Garcia de Arquer, *et al.*, Binding site diversity promotes CO_2 electroreduction to ethanol, *J. Am. Chem. Soc.*, 2019, **141**, 8584–8591.

64 P.-P. Yang, X.-L. Zhang, F.-Y. Gao, Y.-R. Zheng, Z.-Z. Niu, X. Yu, R. Liu, Z.-Z. Wu, S. Qin and L.-P. Chi, *et al.*, Protecting Copper Oxidation State via Intermediate Confinement for Selective CO_2 Electroreduction to C_{2+} Fuels, *J. Am. Chem. Soc.*, 2020, **142**, 6400–6408.

65 F. Li, A. Thevenon, A. Rosas-Hernández, Z. Wang, Y. Li, C. M. Gabardo, A. Ozden, C. T. Dinh, J. Li and Y. Wang, *et al.*, Molecular tuning of CO_2-to-ethylene conversion, *Nature*, 2020, **577**, 509–513.

66 C. M. Gabardo, C. P. O'Brien, J. P. Edwards, C. McCallum, Y. Xu, C.-T. Dinh, J. Li, E. H. Sargent and D. Sinton, Continuous carbon dioxide electroreduction to concentrated multi-carbon products using a membrane electrode assembly, *Joule*, 2019, **3**, 2777–2791.